ACS OMEGA

Open Access

http://pubs.acs.org/journal/acsodf

Article

Anomalous Temperature-Induced Particle Size Reduction in Manganese Oxide Nanoparticles

Alfian Noviyanto,* Ratih Amalia,▽ Pramitha Yuniar Diah Maulida, Mudzakkir Dioktyanto, Bagas Haqi Arrosyid, Didik Aryanto, Lei Zhang, Andrew T. S. Wee, and Arramel*

Cite This: *ACS Omega* 2023, 8, 45152−45162

Read Online

ACCESS | Metrics & More | Article Recommendations | Supporting Information

ABSTRACT: The intricate role of temperature in the structure−property relationship of manganese oxide nanoparticles (Mn_3O_4 NPs) remains an open question. In this study, we successfully synthesized Mn_3O_4 NPs using the hydrothermal method with two differing temperatures, namely, 90 and 150 °C. Interestingly, a smaller average particle size is found when Mn_3O_4 NPs are synthesized at 150 °C compared to 90 °C, corresponding to 46.54 and 63.37 nm, respectively. This was confirmed by the time variation of temperature setting of 150 °C where the size evolution was insignificant, indicating a competing effect of nucleation and growth particles. Under varying NaOH concentrations (2−6 M) at 150 °C, a reduction in the particle size is found at the highest NaOH concentration (6 M). The particle grows slightly, indicating that the growth state is dominant compared to the nucleation state at low concentrations of NaOH. This finding implies that the high nucleation rate originates from the excessive monomer supply in the high-temperature reaction. In terms of crystallinity order, the structural arrangement of Mn_3O_4 NPs (150 °C) is largely decreased; this is likely due to a facile redox shift to the higher oxidation state of manganese. In addition, the higher ratio of adsorbed oxygen and lattice oxygen in Mn_3O_4 NPs at 150 °C is indirectly due to the higher oxygen vacancy occupancies, which supported the crystallinity decrease. Our findings provide a new perspective on manganese oxide formation in hydrothermal systems.

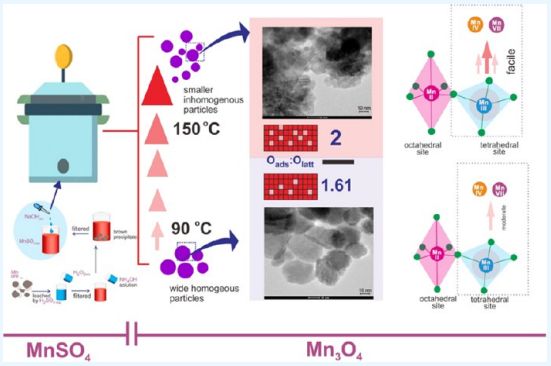

INTRODUCTION

Manganese oxides have various applications in many fields, such as ionic adsorbents,[1] catalysis,[2] supercapacitors,[3] and batteries.[4] In addition to being an environmentally friendly and relatively low-cost material, the wide range of technological applications of manganese oxide is due mainly to the diversity of structures and oxidation numbers of the materials. Manganese oxides could exist in various types (i.e., MnO, MnO_2, Mn_2O_3, Mn_3O_4, and Mn_5O_8) with mixed-valence complexes consisting of different oxidation states $(Mn_2^{2+}Mn^{3+})O_4$ for Mn_3O_4 and $(Mn^{2+})_2(Mn^{4+})_3O_8$ for Mn_5O_8. Among these forms, Mn_3O_4 is considered to be more stable, possessing a flexible structure and ease of fabrication, making it promising for supercapacitor applications in the electrochemical field.[5]

Practically, the fabrication of manganese oxide has been explored through various methods. Several different precursors, such as $MnSO_4$, $KMnO_4$, H_2SO_4, or $K_2S_2O_8$, have been proven to affect the oxide allotrope, size, and crystal structure.[6−10] Another study reported that the hydrothermal oxidation process resulted in pure single-phase spinel-tetragonal Mn_3O_4.[11] Spherical manganese oxide with average sizes in the range of 36−39 nm was obtained through an ultrasonic irradiation-assisted coprecipitation method.[3] Manganese oxide nanowires were successfully synthesized by solvothermal treatment in a polyol system for 24 h.[12] Hausmannite thin films were prepared by a chemical spray pyrolysis technique with the size of 49 ± 0.3 nm and a calculated microstrain of 5.29×10^{-3}.[13] One-dimensional Mn_3O_4 nanorods were obtained by high-temperature calcination of MnOOH.[14] Recently, several works on low-temperature-assisted methods[7,15,16] have been reported, such as the irregular block shape of Mn_3O_4 by the hydrothermal method at 180 °C[17] and monodispersed Mn_3O_4 tetragonals with highly regular walls using a simple mild solution route at 60 °C.[18]

Various methods to fabricate metal oxide nanoparticles have been widely introduced in nanomaterial applications, such as hydrothermal, coprecipitation, solid-state reaction, sol−gel process, thermal decomposition, and the two-phase hydrolysis approach.[18−20] Hydrothermal synthesis is preferred among the others, which gives rise to the positive properties in

Received: October 13, 2023
Revised: October 28, 2023
Accepted: November 1, 2023
Published: November 13, 2023

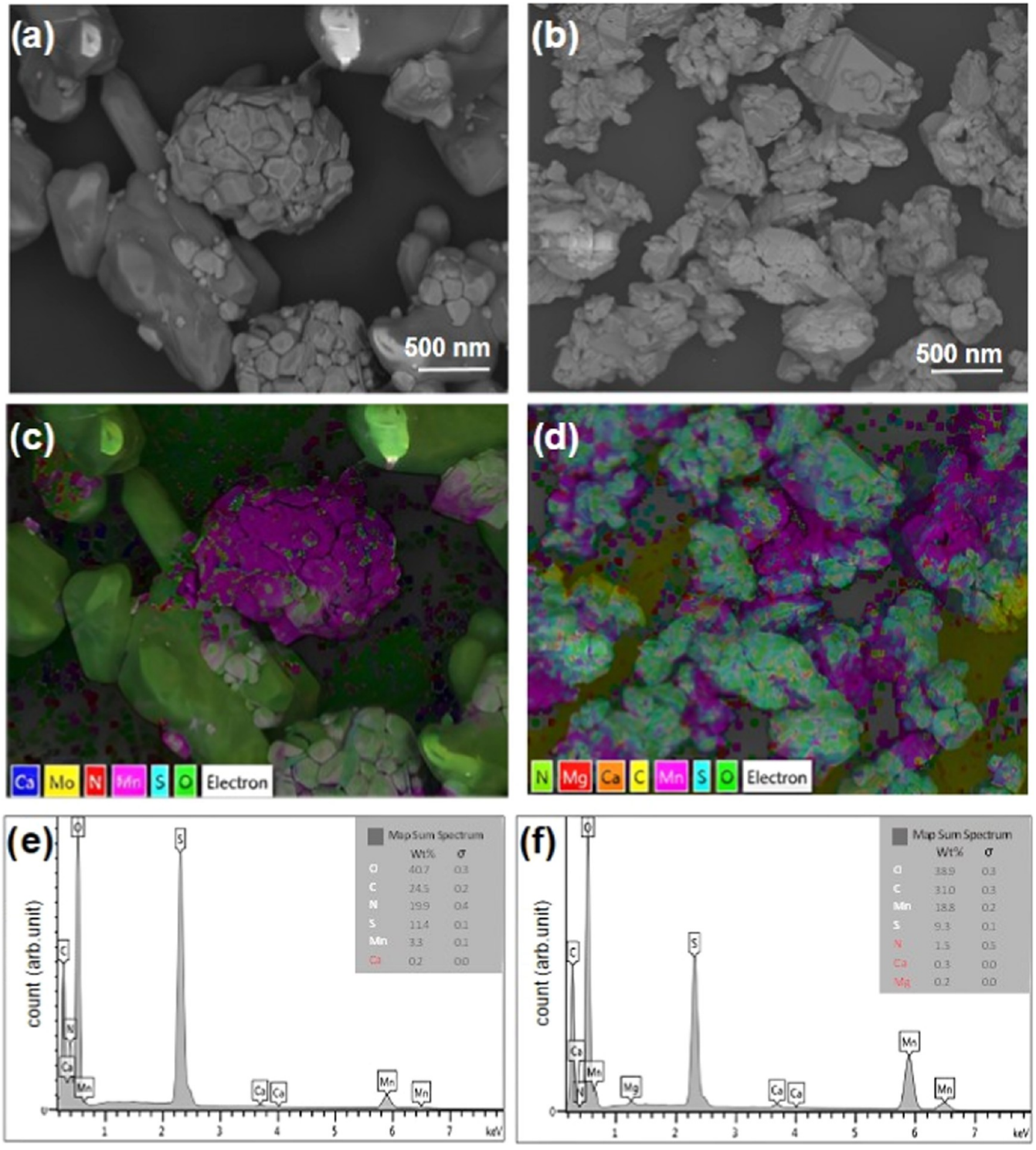

Figure 1. SEM images and mapping of elemental analyses of manganese sulfate obtained from (a) the manganese ore and (b) commercial samples. (c, d) EDS mappings from the respective manganese ore and commercial samples. (e, f) EDS mappings from the elemental percentage in MO90 and MO150.

nanoparticle synthesis due to its simple preparation, low energy, fast reaction, smaller particle size, and pure particle form.[21] In the hydrothermal process, size is strongly influenced by three parameters, namely, nuclei formation, temperature, and supersaturation. The first of the two mentioned are the most significant factors affecting the nucleation rate of nanoparticles.[22] Temperature or any "heating-up"[22] methods play an important role in the determination of the critical radius of nuclei, serving as a template for particle growth due to the increase of the total free energy. However, unlike the "hot-injection" process, where the underlying mechanism has been well-studied through rapid injection to stimulate an instant supersaturation,[22] the underlying mechanism of size distribution control in the hydrothermal method has not been satisfactorily explained. Indeed, previous studies have proposed several mechanisms within the phenomenon in hydrothermal

https://doi.org/10.1021/acsomega.3c08012
ACS Omega 2023, 8, 45152−45162

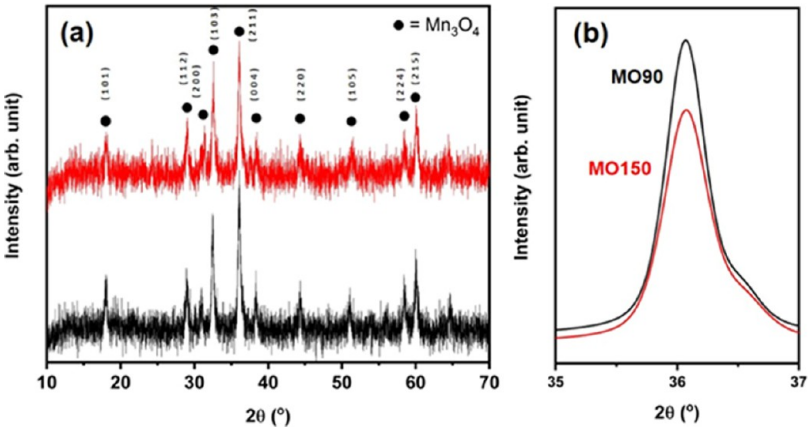

Figure 2. X-ray diffraction pattern of (a) ore-derived Mn_3O_4 obtained from the hydrothermal process at 90 (black) and 150 °C (red). (b) XRD peak intensity comparison at 36.06°.

Table 1. XRD Parameter of the Synthesized Mn_3O_4 Nanomaterial by Temperature Variation

temperature (°C)/time (h)	lattice parameter (Å)			crystallinity (%)	crystallite size (nm) − Scherrer equation	particle size (nm) - SEM
	a	*b*	*c*			
90/18	5.767	5.767	9.386	55.33	31.12	75.23 ± 1.42
150/1	5.772	5.772	9.361	79.59	28.77	42.36 ± 1.06
150/6	5.780	5.780	9.246	59.95	23.55	49.34 ± 0.75
150/18	5.774	5.774	9.364	50.35	27.02	57.87 ± 1.88

systems, such as the MnO_2 growth mechanism through shape evolution by increasing the precursor concentration,[23] hematite nanoparticle growth by different types of intermediate phases,[24] and iron-oxide nanoparticle growth by kinetic approach as a temperature function, which mostly supports the common trend of increased particle size.[22] However, the opposite trend was also found in the synthesis of ZrO_2 when the crystallite size reduction is mainly due to a higher active site (seed) introduced by a larger chemical reaction.[25] To the best of our knowledge, the proposed mechanism underlying the opposite trend of size evolution in manganese oxide formation is still scarce.

As the physicochemical properties of Mn_3O_4 are highly dependent on the structure, a structural design is considered to be a determinant factor of efficiency, especially in electrochemical applications. Structure modification of Mn_3O_4 could be achieved by adjusting various aspects, such as grain size[26] and particle size.[24,27,28] Studies have shown that grain size, along with the crystal growth direction, could affect the redox reaction and promote the active surface site for oxide metal formation, which correlates with the reactivity in an electrochemical system.[5,26,29] Studies have also reported on the effectiveness of smaller particle size for enhancing the catalytic and mechanical properties of Mn_3O_4 due to the higher surface area.[24,27,28] Crystal quality detail also useful to determine the correlation between the defect structure of a material and the oxygen vacancy,[30] which is useful for providing the surface site in an oxide metal. Several studies have confirmed this finding through XPS analysis by calculating the ratio of the lattice and adsorbed oxygen.[26,29,30]

This study focuses on temperature, a physical parameter, during the hydrothermal method of Mn_3O_4 NP fabrication. The raw materials were collected from Sumbawa manganese ore and treated at a relatively low heating point (90 and 150 °C). We observed its influence on particle size, shape, and crystallinity. Detailed characterizations were conducted through analysis of crystallinity by X-ray diffraction (XRD) and morphology and particle size by scanning electron microscope (SEM) and transmission electron microscope (TEM) profiles. Surface-sensitive techniques, such as XPS, are carried out for the oxidation state elucidation of products at each temperature set point. In addition, we propose a structural insight to interpret the growth mechanism of manganese oxide nanoparticles based on the resulting phenomenon.

RESULTS AND DISCUSSION

As manganese sulfate ($MnSO_4$) plays an important role in supplying Mn from the ore to the final result of manganese oxide, the success of $MnSO_4$ synthesis needs to be evaluated to observe its physicochemical characteristics. This study uses manganese ore from Sumbawa as the starting material and commercial $MnSO_4$ as a comparison. As depicted in Figure 1, both commercial and manganese ores show the presence of $MnSO_4$. The sample obtained from the manganese ore (Figure 1(a)) displays a more concentrated aggregate, as shown by the orange and red lines. On the other hand, commercial $MnSO_4$ has a smaller and more homogeneous particle distribution, as shown in Figure 1(b). It is apparent that $MnSO_4$ from the manganese ore is more centralized than the well-distributed particle from the commercial source. Indeed, commercial $MnSO_4$ possesses higher amounts of Mn (19.9%) compared to those obtained from the manganese ore (3.3%). However, the $MnSO_4$ from the ore contains a small amount of impurities. Due to this, manganese sulfate derived from the manganese ore is considered sufficiently effective for Mn_3O_4 synthesis in this investigation.

In the present study, Mn_3O_4 was prepared by the hydrothermal method under two distinct heating temperatures at 90 (hereafter labeled as MO90) and 150 °C (MO150). The diffraction patterns (Figure 2a) reveal peaks at 2θ of 18, 29, 33,

https://doi.org/10.1021/acsomega.3c08012
ACS Omega 2023, 8, 45152−45162

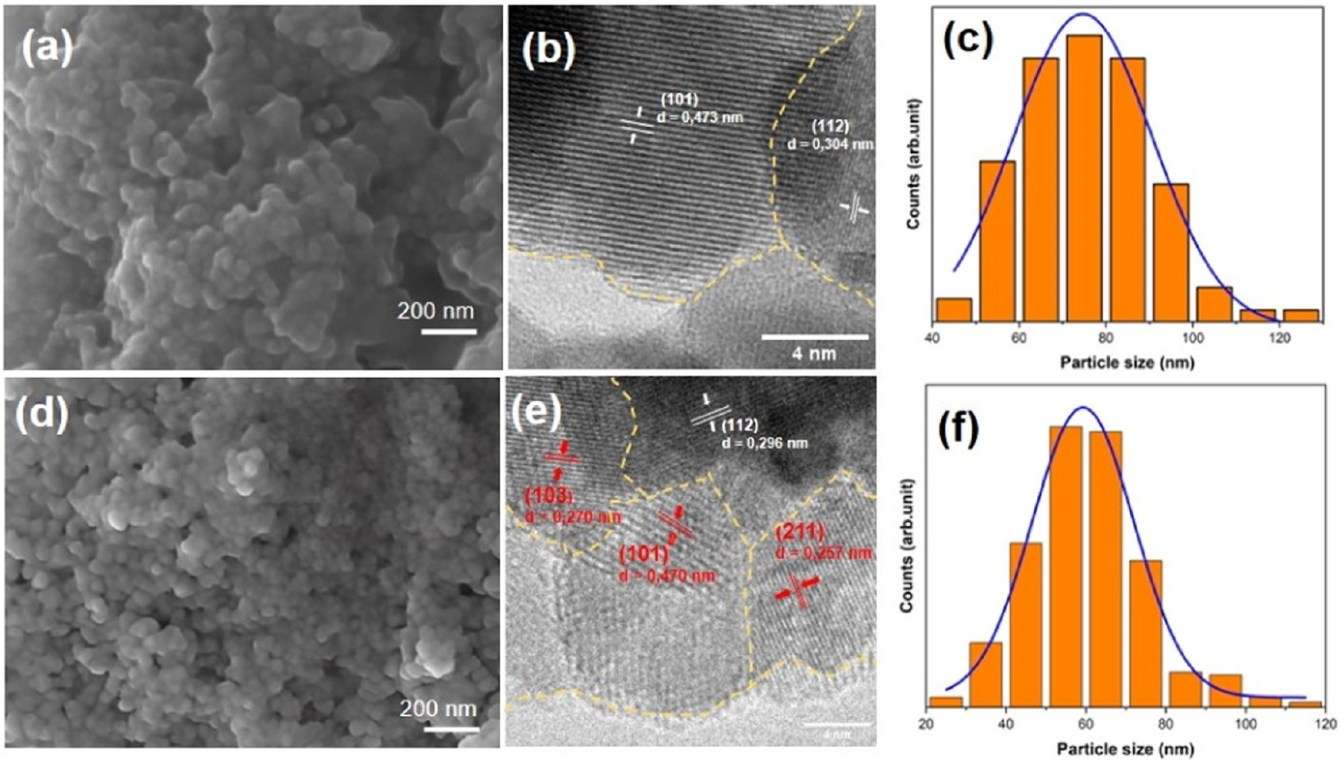

Figure 3. (a) SEM images, (b) TEM profile with the respective interlayer distance, and (c) particle size distribution of MO90 after the hydrothermal method for 18 h. In comparison, MO150 has (d) a smaller particle size morphology in SEM images, (e) a lower interlayer distance, and (f) a distribution of particles.

36, 38, 45, 52, 60, and 65° attributed to the Miller indices of (101), (112), (103), (211), (004), (220), (105), (224), and (400), respectively, confirming the hausmannite phase of the Mn_3O_4 spinel structure.[3] The formation of Mn_3O_4 was also confirmed by Raman spectra, as shown in Figure S1. Raman spectra showed a strong peak at 658 cm^{-1}, which correlated with hausmannite-Mn_3O_4, characterized by sharp and narrow instead of broadening peaks, indicating the absence of MnO_2. The sequence of peaks at 314, 361, and 652 cm^{-1} may be attributed to Mn_3O_4 rather than Mn_2O_3.[20,31−33] The strongest peak (~650 cm^{-1}) can be assigned to the asymmetric stretching mode of bridging oxygen species (Mn−O−Mn),[34,35] which also slightly shifts to a lower figure in MO150. This is in line with the lower grain size of MO150, where this correlation is also found in the literature.[33]

The tetragonal structure of Mn_3O_4 is supported by the extracted lattice parameters, as summarized in Table 1. This is comparable to the standard ICDD 01-089-4837 ($a = b = 5.762$ Å, $c = 9.46$ Å). As shown in Table S1, the refinement parameters show that the good fit (GoF) was less than 4, indicating that the calculation is in agreement with the observed data. According to Table S1, the lattice parameters were determined by Rietveld refinement, with the lattice parameters (a and b) for MO90 being relatively similar to the standard data; however, the difference becomes larger in the case of MO150. These findings are interesting, and we will discuss them further in the following section.

In general, the crystallinity of manganese oxide will increase with temperature due to the faster crystal growth rate. However, in this study, MO150 is shown to have a lower crystallinity than MO90, and both were heated for 18 h. Figure 2b displays the lower peak intensity at 36.05° of MO150 compared to that of MO90, with a relatively constant full width at half-maximum (FWHM) area at 0.37 ± 0.001 nm. Additionally, Mn_3O_4 is also supposed to be highly stable up to ±300 °C before undergoing phase transition at the temperature range of 450−500 °C,[36] which aligns with the absence of other new diffraction peaks. Therefore, this peculiar occurrence opens more discussions on the behavior of Mn_3O_4 when the reaction mixture is heated at a relatively low-temperature range.

Moreover, the crystallite size of MO150 is smaller than that of MO90, further confirming the reduced crystallinity as the temperature reaction is raised (Table 1). The crystallite size was determined by following the Scherrer equation, as shown in eq 1.

$$D = \frac{K}{B \sin \theta} \tag{1}$$

where D is the crystallite size, K is a constant (0.9), λ is the wavelength of the X-ray, B is the FWHM of the observed peak, and θ is the Bragg angle. The crystallite sizes were 31.12 and 27.02 nm for MO90 and MO150, respectively, as shown in Table 1. We also compared the crystallite size determination using the Williamson−Hall method[3,37] and observed a similar trend comparable to the Scherrer equation, as shown in Table S1. The Williamson−Hall plot is shown in Figure S2, where the values of the strain (ε) as a slope and intercept ($k\lambda/D$) were calculated by linear fitting of $4\varepsilon \sin\theta$ vs $\beta_t \cos\theta$. β_t denotes strain broadening and ε denotes microstrain as shown in eq 2.

$$\beta_t \cos\theta = \frac{k\lambda}{D} + 4\varepsilon \sin\theta \tag{2}$$

https://doi.org/10.1021/acsomega.3c08012
ACS Omega 2023, 8, 45152−45162

Table 2. Published Work of Oxides Prepared by Several Methods, Especially Hydrothermal, for Comparable Temperature Range Variation

				result trend as temperature increases	
source	synthesized material	method	temperature range (°C)	particle size	crystallinity
Zhao et al.[6]	MnO	hydrothermal	100−160	-	increase
Liu et al.[7]	Mn_3O_4	hydrothermal	60−180	similar	increase
Wu et al.[44]	MnO	hydrothermal	100−175	increase	-
Liang et al.[45]	MnO	hydrothermal, electrolysis	60−150	increase	increase
Haris et al.[46]	Manganese oxide nanowires	hydrothermal	200−250	increase	increase
Dunne et al.[47]	Fe_2O_3	hydrothermal	200−400	increase	-
Liu et al.[48]	$LiMnO_4$	hydrothermal	70−190	increase	increase
Lester et al.[49]	Co_3O_4	hydrothermal	200−430	increase	-
Wang et al.[17]	$Al(OH)(H_2BTEC)\cdot(H_2O)$	hydrothermal	120−240	increase	increase
Malligavathy et al.[50]	TiO_2	hydrothermal	120−180	similar	increase
Xia et al.[51]	SiOC	solvothermal	140−180	increase	-
Yamada et al.[52]	$BaTiO_3$	solvothermal	150−200	increase	increase
Lin et al.[53]	$Mn_xZn_{1-x}Fe_2O_4$	solvothermal	160−220	increase	increase
Biswas et al.[15]	MnS	solvothermal	60−250	increase	increase
this work	Mn_3O_4	hydrothermal	90−150	decrease	decrease

We believe that the smaller crystallite size following the decrease in crystallinity indicates some restrictions in crystal growth. This trend of smaller crystallite size was also found in the ZrO_2 formation at sizes of 5.9−3.7 nm for 220 and 270 °C due to the larger active site (seed) for particle formation.[25] The microstrain value (Table S1) correlates with the deformative aspects that are present within the material such as dislocations, line defects, and cleavages. These imperfections then cause the crystal growth to be inhibited.[3,13,37−39] Interestingly, an imperfection in the crystallization at higher temperatures results in a significantly larger structural disorder, evident in the 10-fold increase of strain (ε) at 150 °C compared to that at 90 °C. In hydrothermal processes, such a strained crystal might be caused due to lattice oxygen vacancy or a facile redox shift in the crystal structure, as observed in cerium oxide.[47] Therefore, the heating processes support the incremental changes of microstrain, resulting in a deformative structure of crystal quality.[5,29,40,41]

SEM images of MO90 and MO150 are presented in Figure 3(a),3(d), showing a perfectly spherical morphology for MO150, in comparison to the pseudospherical shape in MO90. A significant particle size decrease is also observed, where MO90 and MO150 each have average particle sizes of 75.23 ± 1.42 and 57.87 ± 1.88 nm, respectively. These two microscopy details imply that temperature greatly influences the size and morphology of manganese oxide. The t test was also performed to determine whether the average particle size of MO90 and MO150 is significantly different or not. As shown in Table S3, the $t_{calculated} > t_{table}$; thus, the null hypothesis is rejected. This implies that the average of MO90 and MO150 is significantly different. Further, the TEM profile of MO90 (Figure 3(b)) shows a sharper and clearer lattice compared to the blurred and evenly dispersed MO150 (Figure 3(e)). The interplanar distance analysis also depicted a reduction trend from 0.306 to 0.296 nm (d_{112}) and from 0.473 to 0.470 nm (d_{101}) for MO90 and MO150, respectively. The numerous grain boundaries generated by the smaller particles of MO150 (Figures 3(d) and S3) can provide more active sites for the oxidation reaction, as will be further discussed in the XPS analysis.

Table 2 shows a comparison with the published reports on the synthesis of other nanoparticles that are mainly prepared by the hydrothermal method. Indeed, we find that temperature mostly governs the particle growth direction, which causes the particle size to increase, as reported by various literature works (Table 2). However, we also note a similar observation of an unusual trend that was also reported by Machoke et al. related to the synthesis of Al-zeolite using the hydrothermal method with spray-drying and steam-assisted crystallization.[42] According to their results, the particle sizes are deduced varying from 120 and 40 nm for heated samples at 300 and 400 °C, respectively.[42] A similar case was reported by Fievet et al.,[43] where the sizes of nickel, cobalt, and copper decreased along with the temperature increasing, all falling below 200 °C and suggesting a higher saturation level in such a polyol system during the hydrothermal process. In our system, the saturation level is as low as 150 °C, resulting in high solubility among metal salt, distilled water, and reducing agent NaOH.

We propose that particle size reduction might be related to the hydrolysis event of the corresponding metal salt. As the temperature in the hydrothermal process increases, water in the system reaches the supercritical state, promoting water dissociation. This would lead to hydrolysis of the metal salt, and subsequent nanoparticles will precipitate and form the solution. Extensive precipitation promotes smaller nuclei to be produced, thereby resulting in a smaller particle size.[47] This greater nucleation rate is also evidenced by the thermodynamic approach to particle growth. Based on the Arrhenius equation (eq 3), where I is the nucleation rate and refers to yield/time, E is the nucleation activation energy, A is the preexponential factor, and C is the cluster concentration, the graph ln I will represent the nucleation rate versus $1000/T$, showing that the nucleation rate increases with a higher temperature in our system.

$$\ln I = -\frac{Ea}{RT} + \ln A + \ln C \tag{3}$$

Additionally, the particle size distribution (Figure 3(c),3(f)) shows a more inhomogeneous and broadened distribution for MO150, while MO90 exhibits a narrower distribution. This has been further explained through the Ostwald ripening

https://doi.org/10.1021/acsomega.3c08012
ACS Omega 2023, 8, 45152−45162

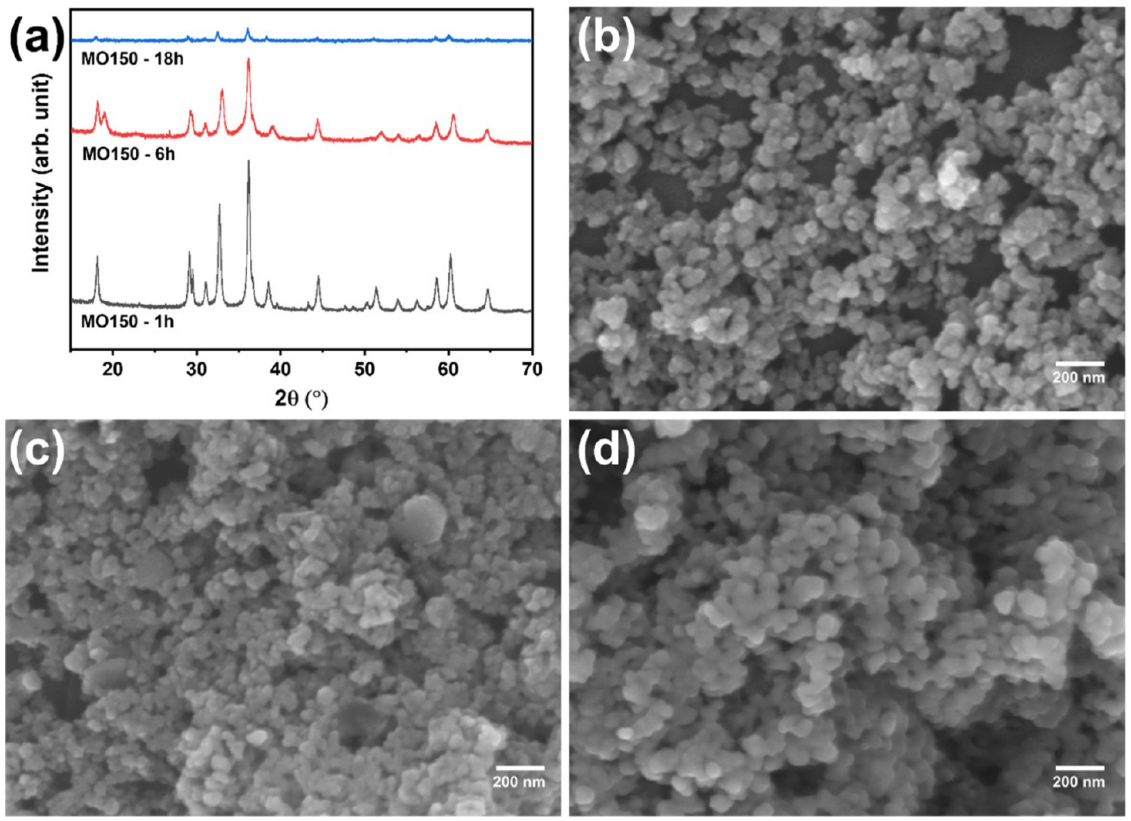

Figure 4. (a) XRD patterns of the MO150 NPs and its corresponding SEM images for (b) 1, (c) 6, and (d) 18 h.

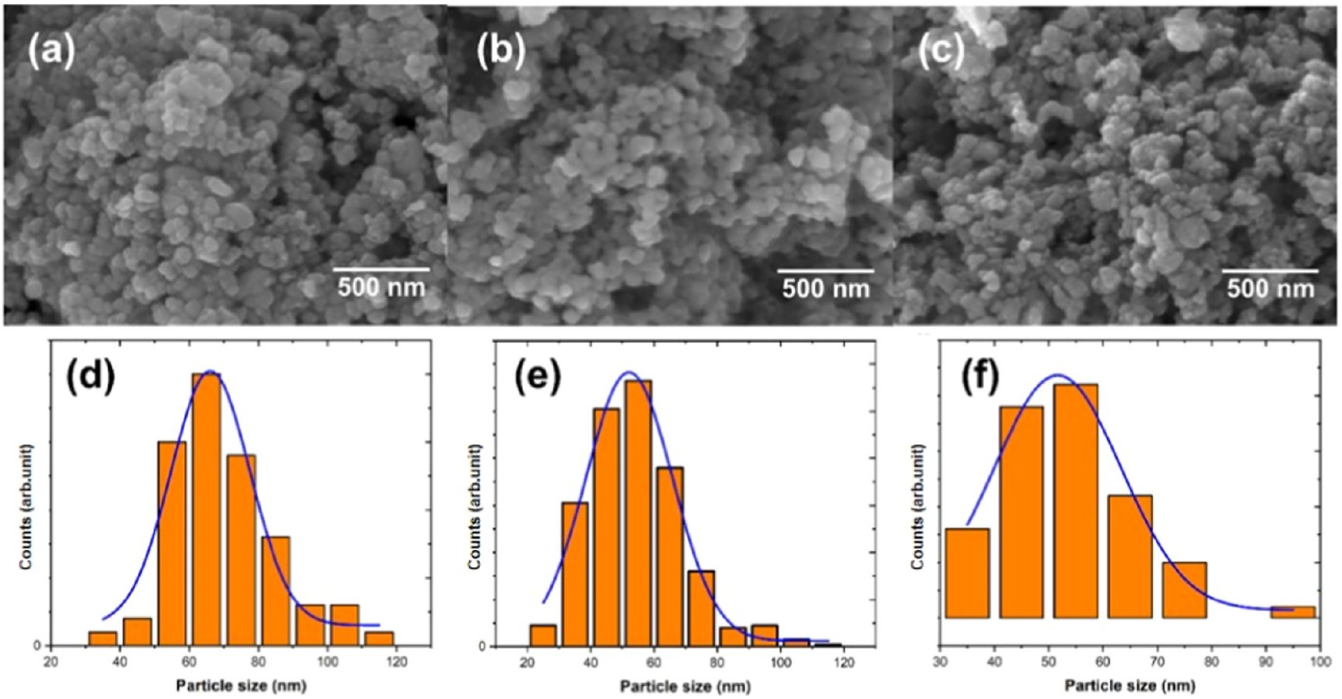

Figure 5. SEM images of Mn_3O_4 NPs synthesized by the hydrothermal process of MO150 for 18 h with NaOH concentrations of (a) 2, (b) 4, and (c) 6 M, and its distribution in (d), (e), and (f), respectively.

mechanism, in which two regimes of self-sharpening and broadening distribution have been well-demonstrated;[54] in other words, more homogeneous particles were obtained through distinct separation of the nucleation state and growth state. This could be rationalized through the LaMer mechanism of nanoparticle formation, which is defined as the accumulation of monomers in the early stages, followed by short burst nucleation with subsequent particle growth. However, this has been difficult to clarify due to the coexistence of both stages.[22,55] Hence, the smaller size of

https://doi.org/10.1021/acsomega.3c08012
ACS Omega 2023, 8, 45152−45162

MO150 is associated with a greater nucleation rate, leading to the preferred formation of heterogeneous particles, which simultaneously support the growth process. On the other hand, this effect somewhat hindered MO90 due to the possibility of terminated nucleation, resulting in more homogeneous particles as illustrated by Figure 6.

To investigate further, we carried out a deeper investigation of the crystal growth mechanism at 150 °C by varying the reaction time. Figure 4(a) displays the XRD diffraction pattern of MO150 heated with varying reaction times from 1 to 18 h. The peak shift was not observed in the diffraction patterns, indicating that the heating period does not affect the formation of the crystal phase. However, a prolonged heating period significantly affects the peak intensity of XRD, where Mn_3O_4 heated for 1 h exhibits more pronounced and sharper peaks than those heated at a longer duration. This phenomenon further confirms that prolonged heating has a detrimental effect on the crystallinity within the structure. On a similar note, Table 1 shows an increase in the microstrain value accompanied by a decrease in the crystallinity and crystallite size as the heating period is increased from 1 to 18 h. The increase in microstrain is indicative of the formation of strained phases, which induce defects within the structure, hence leading to the reduced crystallinity. These phenomena support the calculation from XRD and Rietveld refinements, suggesting that high temperatures facilitate defect formation.

Furthermore, an increase in the hydrothermal duration promotes grain growth, resulting in bigger average particle sizes shown in the SEM profile (Figure 4(b–d)) of 49.11, 42.31, and 65.07 nm for 1, 6, and 18 h, respectively, as shown in Figure S4. However, this effect is not deemed significant, as particle size differences in a similar study were reported as ∼30, 50, and 200 nm for a comparable duration.[24] It is suggested that a highly nucleation-biased process does exist, which inhibits particle growth during reaction at this temperature. The competition between nucleation and grain growth is thought to be the reason for the relatively similar grain size.[47]

As mentioned above, the formation of monomers could also affect particle growth. In the current study, the use of NaOH as a reducing and precipitating agent during the hydrothermal process is investigated. Therefore, the influence of monomer formation on the particle size of Mn_3O_4 is carried out by varying NaOH concentrations. Figure 5 shows the SEM images of Mn_3O_4 NPs as a function of NaOH concentration. Figure 5d–f displays the smallest particle size of Mn_3O_4 found at a high concentration. Average particle sizes of 69.85, 54.26, and 53.34 nm are obtained for 2, 4, and 6 M, respectively.

This phenomenon could be attributed to reduced particle growth due to the abundant monomer supply. Metal oxide nanoparticles are formed by an olation mechanism through a hydroxy bridge in an aqueous solution by a condensation reaction.[22] As the hydroxylated metal is not stable, the hydroxide ion from NaOH will act as a ligand. The condensation process was then followed by the nucleophilic attack of − OH through the hydroxyl bridge and water elimination. Hence, $[M(OH)_h(OH_2)_{6-h}]$ emerges as the new monomer.[54] The monomer supply continues to increase until the solution reaches a supersaturation level, in which nuclei will start to form, followed by the growth stage to generate bigger particles through the dissolution of smaller clusters or remaining monomers in the solution. The nucleation process persists as long as the system is at a supersaturation level as a result of the high monomer supply.[22] According to this process, NaOH promotes nucleation via the formation of $Mn(OH)_2$. Therefore, a higher amount of NaOH promotes a higher rate of monomer supply; consequently, the nuclei formation will be more prevalent, and smaller particles are most likely formed due to the lower availability of the precursor during particle growth. This phenomenon was also observed in other metal oxides, such as hematite, with NH_4OH acting as the precipitating agent.[24] In addition, Figure 5c,f display a broadening distribution of particle sizes, indicating that heterogeneous particles are formed when a high NaOH concentration is used. This could be explained by the high amount of monomer supply, which causes the nuclei formation to persist, concurrent with particle growth. The overall proposed mechanism of the developed Mn_3O_4 NPs by the hydrothermal process is depicted in Figure 6.

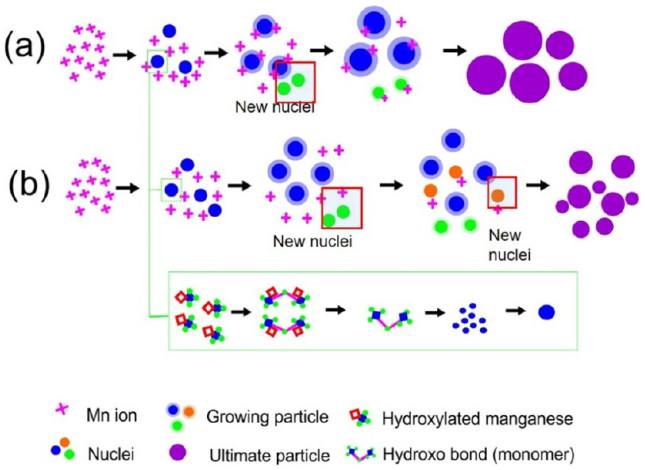

Figure 6. Schematic illustration of the nucleation and growth of Mn_3O_4 NPs for (a) MO90 and (b) MO150. The more simultaneous nucleation and growth stage occurs at 150 °C, and more distinct separation in those stages possibly occurred at 90 °C; hence, bigger and homogeneous particles of MO90 were obtained, while in the former stage, smaller and heterogeneous particles were obtained.

As the temperature strongly affects the particle characteristics, further investigation was conducted by means of surface-sensitive XPS analysis. The core levels of Mn 3s, O 1s, Mn 2p, and Mn 3p were obtained by the XPS survey scans (Figure 7(a)). The absence of sulfur (S) unambiguously indicated profound complete reaction of $MnSO_4$ consumption or that impurities were successfully removed during the rinsing process. This means that the chemical purity of as-obtained Mn_3O_4 is relatively high even though the precursor was obtained from a manganese ore. The Mn 2p peak shows multiple splitting into Mn $2p_{1/2}$ and Mn $2p_{3/2}$, with a splitting peak distance at about 11.5 eV, in accordance with previous studies.[3,13,39,56,57] In order to elucidate Mn species with different oxidation states, further deconvolution of the Mn 2p suggests four different species of manganese cations spanning in the ranges of 638.84–640.91, 641.35–642.24, 643.69–643.69, and 645.94–645.87 eV. These values correspond to the different oxidation states of Mn^{2+},[3,58] Mn^{3+},[59,60] Mn^{4+},[3,59] and Mn^{7+},[60,61] respectively. We attributed the extracted binding energies to compounds such as MnO or $Mn(OH)_2$,[3,58] Mn_2O_3 or Mn(OOH),[58,60] MnO_2, and MnO_4^-, respectively.

In general, the manganese species in MO90 is dominated by Mn^{3+} and Mn^{2+}, while MO150 has the lowest amount of Mn^{3+},

https://doi.org/10.1021/acsomega.3c08012
ACS Omega 2023, 8, 45152−45162

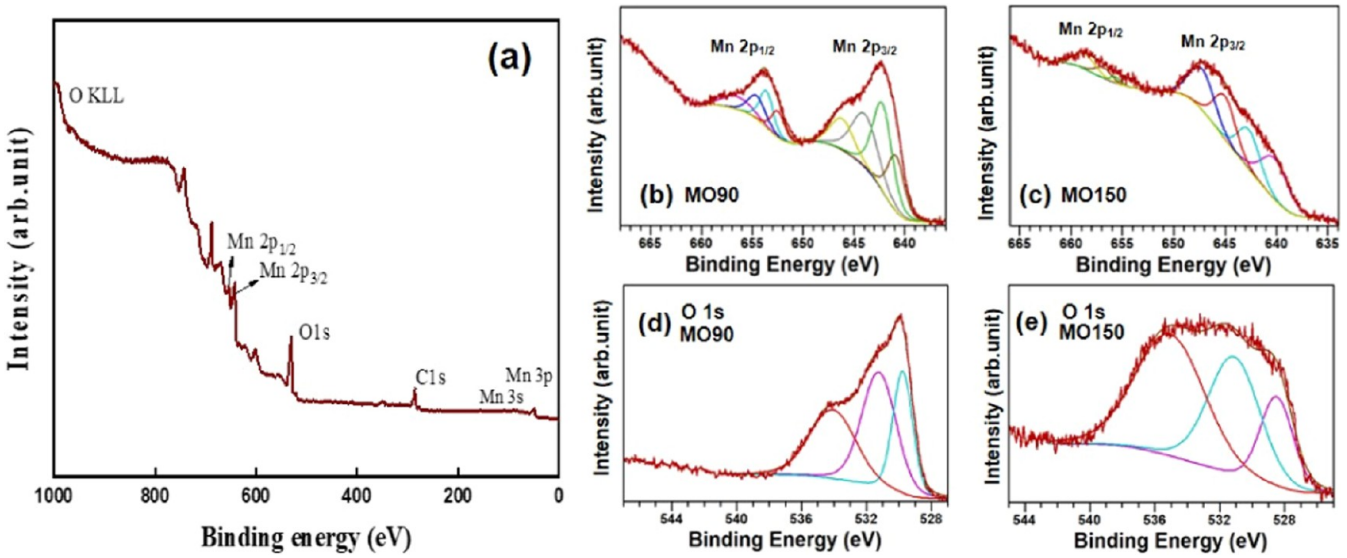

Figure 7. (a) XPS survey spectrum of synthesized Mn_3O_4. Fitted XPS spectra of deconvolution of Mn 2p of (b) MO90 and (c) MO150. Deconvolution of O 1s for (d) MO90C and (e) MO150.

with a corresponding increase in proportion of Mn^{4+} and Mn^{7+}. These indicate that the low valence state of Mn is more accessible at low temperatures, while a higher oxidation state of Mn dominates at 150 °C. Two plausible chemical forms of Mn_3O_4 as bivalence of Mn are MnO_2-2MnO[3,13,60−62] with an area ratio of Mn^{2+}/Mn^{4+} at ∼1.33 or MnO-Mn_2O_3 with the ratio of Mn^{2+}/Mn^{3+} at 1.8−2.[59] According to this study, we propose that the former cases share similarity to MO90 and MO150, with the mixed-valence ratios of 1.13 and 1.18, respectively. This data is also consistent with the chemical shift, wherein Mn^{4+} had a more prominent role than Mn^{3+} in distribution intensity within the octahedral site of the crystal structure (Table S4).

The heating process can be considered a closed system that likely encourages the oxidation effect.[27,30] Based on the literature, the manganese species for manganese oxide with the $MnSO_4$ precursor usually comprises Mn^{2+}, Mn^{3+}, and Mn^{4+} as the highest oxidation states.[3,13,36,63] The higher valence of Mn, such as Mn^{5+}, Mn^{6+}, and Mn^{7+}, is considered to be less stable.[56,59] The signature Mn^{7+} in this work is considered to exist due to the ex situ oxidation process that may occur along with aging. Hausmannite consists of Mn^{2+} occupancy in the octahedra site and correlates with the d^5 state, which is very stable due to the half-filled orbital rule. On the other hand, the Mn^{3+} species occupy the tetrahedral site with the d^4 state in high spin, leading to several discrepancies, such as oxygen vacancy and crystal defects.[34] Additionally, it seems that the oxidation effect occurred selectively, as shown by the significant drop in Mn^{3+} concentration at higher temperatures, while Mn^{2+} remained relatively the same.

The fitting results of XPS O 1s demonstrated that three common oxygen species could be found in MO90 and MO150 samples. These are 528.48−529.5, 531.1−531.21, and 535.06−534.0 eV related to the oxygen lattice (O_{latt}), adsorbed oxygen (O_{ads}), and physisorbed H_2O.[26,64,65] The higher amount of H_2O physisorbed in MO150 (Table S4) is due to the higher reactivity as a result of particle size reduction along with the aging before testing with the ambient conditions. The ratio of O_{ads} and O_{latt} could be an indication of the oxygen adsorption capacity, in which a higher ratio means that more species of active oxygen penetrate the lattice surface of the crystal framework. The ratios of O_{ads} and O_{latt} for MO90 and MO150 are 1.61 and 2.00, respectively, implying that a higher temperature translates to a higher capacity to adsorb active oxygen on the lattice surface. Additionally, further advanced techniques such as positron measurement using a high-resolution synchrotron source could profoundly probe the presence of oxygen vacancy or any defect lattice structure. However, it has been reported that such an indirect approach can be used through increasing the O_{ads}/O_{latt} ratio from deconvoluted XPS, predicting the higher concentration of oxygen vacancy.[64−67] Furthermore, Barbero et al. (2006) observed a similar trend, noting that higher ratio values were correlated to the shift of the higher oxidation state of Fe^{3+} to Fe^{4+}.[68] In addition, oxygen vacancies have been associated with decreased crystallinity and are considered crystal defects.[65] This is also found in metal oxide formations, such as Co_3O_4 or In−Ga−Zn oxide.[29,30] This increased oxygen vacancy, contributing to a decrease in crystallinity as observed in several studies, proves useful in catalytic performances due to the more active sites being available.

CONCLUSIONS

In this paper, we report on an anomalous behavior of the synthesis of Mn_3O_4 NPs from the Sumbawa manganese ore. Based on morphological investigations, we found that crystallinity and particle size were shown to decrease at 150 °C, in contrast to the existing literature. To interpret the findings, two physical origins are proposed: the nucleation state and oxygen vacancy. This strong dominance of nucleation over the growth state is revealed to be due to the small particle size of MO150. In addition, NaOH as a reducing agent can influence the monomer supply during particle formation, resulting in a particle size reduction. Based on the Arrhenius analysis, a higher nucleation rate is realized when the hydrothermal synthesis is carried out at 150 °C. A facile redox shift in this setting temperature occurred, suggesting temperature-induced defects within the structure. We shed some light on the perspective of the unusual mechanism of manganese oxide formation based on the hydrothermal

https://doi.org/10.1021/acsomega.3c08012
ACS Omega 2023, 8, 45152−45162

method, and this might be beneficial for catalytic performances corresponding to the probability of higher active site availability.

EXPERIMENTAL SECTION

Synthesis of Manganese Oxide. Manganese ore from Sumbawa, Indonesia, was used as the starting material. The manganese ore was leached with 4 M H_2SO_4 (purity 95%, Merck) at 70 °C, with the ratio between the solution and the ore being 5:1. Next, to the mixed solution was added 5 g of 0.8 M H_2O_2 carefully and stirred for 90 min. The mixed solution was filtered by using a Buchner vacuum filter to separate the sedimentation and solution. The color of the solution was red wine, and it was mixed with NH_4OH to adjust the pH to 6 to obtain the $MnSO_4$ solution. NaOH with different molarities was added drop-by-drop into the reaction vessel containing $MnSO_4$ with a ratio of 1:1 in volume and stirred for 15 min at ambient temperature. The mixed suspension was moved into an autoclave and heated at 90 (MO90) and 150 °C (MO150) at various times. Then, the precipitate from the hydrothermal process was washed with demineralized water until the pH was neutral, followed by filtering and drying at 105 °C for 2 h.

SEM Imaging. Sample micrographs were taken under 10 kV accelerating voltage in the secondary electron mode using a Jeol JIB-4610F field emission scanning electron microscope (FE-SEM) and equipped with energy-dispersive spectroscopy (EDS). The average particle size of manganese oxide was estimated by measuring the diameter of more than 100 particles with ImageJ software and analyzed statistically.

X-ray Diffraction. X-ray diffraction was performed using a Rigaku MiniFlex 600 with a Cu-Kα source at 40 kV, while the 2θ angle ranged from 5 to 80°.

Transmission Electron Microscope. The TEM image was taken by Tecnai G2 20S-Twin, FEI with acceleration voltage 200 kV.

Raman Spectroscopy. Raman spectroscopy was performed using a DXR3xi Raman imaging microscope from Thermo Fisher Scientific. The laser power was set up to 1 mW, followed by an exposure time of 0.0222 s and 35 scans.

X-ray Photoelectron Spectroscopy. X-ray photoelectron spectroscopy (XPS) was performed on the samples with an impingement area of about 1 mm in diameter using a magnesium Kα X-ray source (excitation energy output of 1254 eV). The oxidation state was elucidated through XPS analysis with CasaXPS software with a range of binding energies from 0 to −1000 eV.

ASSOCIATED CONTENT

Supporting Information

The Supporting Information is available free of charge at https://pubs.acs.org/doi/10.1021/acsomega.3c08012.

Rietveld refinement of XRD diffractograms of Mn_3O_4; Raman spectra of Mn_3O_4; Williamson−Hall plot of MO90 and MO150; and tabulated X-ray photoelectron spectroscopy parameter of Mn 2p and O 1s deconvolution (PDF)

AUTHOR INFORMATION

Corresponding Authors

Alfian Noviyanto − *Nano Center Indonesia, South Tangerang, Banten 15314, Indonesia; Department of Mechanical Engineering, Mercu Buana University, Kebun Jeruk, Jakarta 11650, Indonesia;* orcid.org/0000-0002-6371-6765; Email: a.noviyanto@nano.or.id, alfian.noviyanto@mercubuana.ac.id

Arramel − *Nano Center Indonesia, South Tangerang, Banten 15314, Indonesia;* orcid.org/0000-0003-4125-6099; Email: arramel@nano.or.id

Authors

Ratih Amalia − *Nano Center Indonesia, South Tangerang, Banten 15314, Indonesia*

Pramitha Yuniar Diah Maulida − *Nano Center Indonesia, South Tangerang, Banten 15314, Indonesia;* orcid.org/0000-0003-2082-8182

Mudzakkir Dioktyanto − *Nano Center Indonesia, South Tangerang, Banten 15314, Indonesia*

Bagas Haqi Arrosyid − *Nano Center Indonesia, South Tangerang, Banten 15314, Indonesia*

Didik Aryanto − *Research Center for Advanced Materials, National Research and Innovation Agency, South Tangerang, Banten 15314, Indonesia*

Lei Zhang − *Department of Physics, National University of Singapore, Singapore 117551, Singapore*

Andrew T. S. Wee − *Department of Physics, National University of Singapore, Singapore 117551, Singapore; NUS Graduate School for Integrative Sciences and Engineering, National University of Singapore, Singapore 117456, Singapore; Centre for Advanced 2D Materials and Graphene Research Centre, National University of Singapore, Singapore 117546, Singapore;* orcid.org/0000-0002-5828-4312

Complete contact information is available at: https://pubs.acs.org/10.1021/acsomega.3c08012

Author Contributions

$^{\nabla}$This author contributed equally as the first author. The manuscript was written through the contributions of all authors. All authors have given approval to the final version of the manuscript.

Notes

The authors declare no competing financial interest.

ACKNOWLEDGMENTS

This work was financially supported by the Kerjasama Dalam Negeri Scheme (KDN) [grant number 02-5/658/B-SPK/V/2023], Mercu Buana University. The authors would like to express their gratitude to the Nano Center Indonesia for their facilities and characterization. The authors acknowledge Wong How Kwong for his help with XPS characterization.

REFERENCES

(1) Con, T. H.; Thao, P.; Dai, T. X.; Loan, D. K. Application of Nano Dimensional MnO_2 for High Effective Sorption of Arsenic and Fluoride in Drinking Water. *Environ. Sci.* **2013**, *1* (2), 69−77.

(2) Truong, T. T.; Liu, Y.; Ren, Y.; Trahey, L.; Sun, Y. Morphological and Crystalline Evolution of Nanostructured MnO_2 and Its Application in Lithium-Air Batteries. *ACS Nano* **2012**, *6* (9), 8067−8077.

(3) Tholkappiyan, R.; Naveen, A. N.; Vishista, K.; Hamed, F. Investigation on the Electrochemical Performance of Hausmannite Mn_3O_4 Nanoparticles by Ultrasonic Irradiation Assisted Co-Precipitation Method for Supercapacitor Electrodes. *J. Taibah Univ. Sci.* **2018**, *12* (5), 669−677.

(4) Laffont, L.; Gibot, P. High Resolution Electron Energy Loss Spectroscopy of Manganese Oxides: Application to Mn_3O_4 Nanoparticles. *Mater. Charact.* **2010**, *61* (11), 1268−1273.

(5) Wang, Y.; Zhong, Z.; Chen, Y.; Ng, C. T.; Lin, J. Controllable Synthesis of Co_3O_4 from Nanosize to Microsize with Large-Scale Exposure of Active Crystal Planes and Their Excellent Rate Capability in Supercapacitors Based on the Crystal Plane Effect. *Nano Res.* **2011**, *4* (7), 695−704.
(6) Zhao, H.; Wang, A.; Zhang, Q.; Han, C. Highly Efficient Removal of Ozone by Amorphous Manganese Oxides Synthesized with a Simple Hydrothermal Method. *J. Environ. Sci.* **2023**, *134*, 96−107.
(7) Liu, J. L.; Fan, L. Z.; Qu, X. Low Temperature Hydrothermal Synthesis of Nano-Sized Manganese Oxide for Supercapacitors. *Electrochim. Acta* **2012**, *66*, 302−305.
(8) Zhang, W.; Cheng, C. Y. Manganese Metallurgy Review. Part I: Leaching of Ores/Secondary Materials and Recovery of Electrolytic/Chemical Manganese Dioxide. *Hydrometallurgy* **2007**, *89* (3−4), 137−159.
(9) Li, Y.; Zhou, X.; Zhou, H.; Shen, Z.; Chen, T. Hydrothermal Preparation of Nanostructured MnO2 and Morphological and Crystalline Evolution. *Front. Chem. China* **2008**, *3* (2), 128−132.
(10) Xiao, T. D.; Strutt, P. R.; Benaissa, M.; Chen, H.; Kear, B. H. Synthesis of High Active-Site Density Nanofibrous MnO_2-Base Materials with Enhanced Permeabilities. *Nanostructured Mater.* **1998**, *10* (6), 1051−1061.
(11) Ganesh Kumar, V.; Aurbuch, D.; Gedanken, A. A Comparison between Hot-Hydrolysis and Sonolysis of Various Mn(II) Salts. *Ultrason. Sonochem.* **2003**, *10* (1), 17−23.
(12) Li, F.; Wu, J.; Qin, Q.; Li, Z.; Huang, X. Facile Synthesis of γ-MnOOH Micro/Nanorods and Their Conversion to β-MnO_2, Mn_3O_4. *J. Alloys Compd.* **2010**, *492* (1−2), 339−346.
(13) Moses Ezhil Raj, A.; Victoria, S. G.; Jothy, V. B.; Ravidhas, C.; Wollschläger, J.; Suendorf, M.; Neumann, M.; Jayachandran, M.; Sanjeeviraja, C. XRD and XPS Characterization of Mixed Valence Mn_3O_4 Hausmannite Thin Films Prepared by Chemical Spray Pyrolysis Technique. *Appl. Surf. Sci.* **2010**, *256* (9), 2920−2926.
(14) Yang, Z.; Zhang, Y.; Zhang, W.; Wang, X.; Qian, Y.; Wen, X.; Yang, S. Nanorods of Manganese Oxides: Synthesis, Characterization and Catalytic Application. *J. Solid State Chem.* **2006**, *179* (3), 679−684.
(15) Biswas, S.; Kar, S.; Chaudhuri, S. Growth of Different Morphological Features of Micro and Nanocrystalline Manganese Sulfide via Solvothermal Process. *J. Cryst. Growth* **2007**, *299* (1), 94−102.
(16) Sreenivasa Kumar, G.; Venkataramana, B.; Reddy, S. A.; Maseed, H.; Nagireddy, R. R. Hydrothermal Synthesis of Mn_3O_4nanoparticles by Evaluation of pH Effect on Particle Size Formation and Its Antibacterial Activity. *Adv. Nat. Sci. Nanosci. Nanotechnol.* **2020**, *11* (3), No. 035006.
(17) Wang, F.; Zhu, L.; Wei, Q.; Wang, Y. Research on the Effects of Hydrothermal Synthesis Conditions on the Crystal Habit of MIL-121. *R. Soc. Open Sci.* **2020**, *7* (11), No. 201212.
(18) Wang, N.; Guo, L.; He, L.; Cao, X.; Chen, C.; Wang, R.; Yang, S. Facile Synthesis of Monodisperse Mn_3O_4 Tetragonal Nanoparticles and Their Large-Scale Assembly into Highly Regular Walls by a Simple Solution Route. *Small* **2007**, *3* (4), 606−610.
(19) Seo, W. S.; Jo, H. H.; Lee, K.; Kim, B.; Oh, S. J.; Park, J. T. Size-Dependent Magnetic Properties of Colloidal Mn_3O_4 and MnO Nanoparticles. *Angew. Chem. - Int. Ed.* **2004**, *116*, 1135−1137.
(20) Zhang, P.; Zhan, Y.; Cai, B.; Hao, C.; Wang, J.; Liu, C.; Meng, Z.; Yin, Z.; Chen, Q. Shape-Controlled Synthesis of Mn_3O_4 Nanocrystals and Their Catalysis of the Degradation of Methylene Blue. *Nano Res.* **2010**, *3* (4), 235−243.
(21) Byrappa, K.; Adschiri, T. Hydrothermal Technology for Nanotechnology. *Prog. Cryst. Growth Charact. Mater.* **2007**, *53* (2), 117−166.
(22) Kwon, S. G.; Piao, Y.; Park, J.; Angappane, S.; Jo, Y.; Hwang, N. M.; Park, J. G.; Hyeon, T. Kinetics of Monodisperse Iron Oxide Nanocrystal Formation by "Heating-up" Process. *J. Am. Chem. Soc.* **2007**, *129* (41), 12571−12584.
(23) Duan, X.; Yang, J.; Gao, H.; Ma, J.; Jiao, L.; Zheng, W. Controllable Hydrothermal Synthesis of Manganese Dioxide Nanostructures: Shape Evolution, Growth Mechanism and Electrochemical Properties. *CrystEngComm* **2012**, *14* (12), 4196−4204.
(24) Khalil, M.; Yu, J.; Liu, N.; Lee, R. L. Hydrothermal Synthesis, Characterization, and Growth Mechanism of Hematite Nanoparticles. *J. Nanoparticle Res.* **2014**, *16* (4), 2362.
(25) Stolzenburg, P.; Freytag, A.; Bigall, N. C.; Garnweitner, G. Fractal Growth of ZrO_2 Nanoparticles Induced by Synthesis Conditions. *CrystEngComm* **2016**, *18* (43), 8396−8405.
(26) Chang, Y.; Guo, Y.; Li, M.; Wang, K.; Lv, L.; Liu, D. Effects of Crystal Quality, Grain-Size and Oxygen Vacancy of Nanocrystalline CeO_2 Films under 1.5 MeV Au Ion Irradiation. *J. Nucl. Mater.* **2019**, *518*, 41−47.
(27) Yang, Q. H.; Zhang, Z. Investigation on Preparing Mn_3O_4 Nanopowder by Hydrothermal Reaction Method. *Mater. Res. Innov.* **2015**, *19* (June), S2142−S2146.
(28) Lett, J. A.; Alshahateet, S. F.; Fatimah, I.; Sivasankaran, R. P.; Sibhatu, A. K.; Le, M. V.; Sagadevan, S. Hydrothermal Synthesis and Photocatalytic Activity of Mn_3O_4 Nanoparticles. *Top. Catal.* **2023**, *66* (1−4), 126−138.
(29) Hao, J.; Peng, S.; Li, H.; Dang, S.; Qin, T.; Wen, Y.; Huang, J.; Ma, F.; Gao, D.; Li, F.; Cao, G. A Low Crystallinity Oxygen-Vacancy-Rich Co_3O_4 Cathode for High-Performance Flexible Asymmetric Supercapacitors. *J. Mater. Chem. A* **2018**, *6* (33), 16094−16100.
(30) Hiramatsu, T.; Nakashima, M.; Kikuchi, E.; Ishihara, N.; Tsubuku, M.; Dairiki, K.; Yamazaki, S. Correlation between Crystallinity and Oxygen Vacancy Formation in In-Ga-Zn Oxide. *Jpn. J. Appl. Phys.* **2016**, *55* (2), No. 021203.
(31) Shah, H. U.; Wang, F.; Toufiq, A. M.; Ali, S.; Khan, Z. U. H.; Li, Y.; Hu, J.; He, K. Electrochemical Properties of Controlled Size Mn_3O_4 Nanoparticles for Supercapacitor Applications. *J. Nanosci. Nanotechnol.* **2018**, *18* (1), 719−724.
(32) Xu, H.; Xu, S.; Wang, H.; Yan, H. Characterization of Hausmannite Mn_3O_4 Thin Films by Chemical Bath Deposition. *J. Electrochem. Soc.* **2005**, *152* (12), C803.
(33) Zuo, J.; Xu, C.; Liu, Y.; Qian, Y. Crystallite Size Effects on the Raman Spectra of Mn_3O_4. *Nanostructured Mater.* **1998**, *10* (8), 1331−1335.
(34) Zhang, X.; Zhao, H.; Song, Z.; Zhao, J.; Ma, Z.; Zhao, M.; Xing, Y.; Zhang, P.; Tsubaki, N. Influence of Hydrothermal Synthesis Temperature on the Redox and Oxygen Mobility Properties of Manganese Oxides in the Catalytic Oxidation of Toluene. *Transit. Met. Chem.* **2019**, *44* (7), 663−670.
(35) Post, J. E.; McKeown, D. A.; Heaney, P. J. Raman Spectroscopy Study of Manganese Oxides: Layer Structures. *Am. Mineral.* **2021**, *106* (3), 351−366.
(36) Dhaouadi, H.; Ghodbane, O.; Hosni, F.; Touati, F. Mn_3O_4 Nanoparticles: Synthesis, Characterization, and Dielectric Properties. *ISRN Spectrosc.* **2012**, *2012*, No. 706398.
(37) Ilmi, M.; Setiawan, P.; Maryanti, E. X-Ray Diffraction Peak Profile Analysis for Determination of Microstructural Properties of Hematite (Fe_2O_3). *J. Res. Dev. Nanotechnol.* **2021**, *1* (July), 10−17.
(38) Lee, A. Y.; Erdemir, D.; Myerson, A. S. *Crystals and Crystal Growth*; Myerson, A. S.; Erdemir, D.; Lee, A. Y., Eds.; Cambridge University Press: Cambridge, 2019.
(39) Brice, J. C. Some Thermodynamic Aspects of the Growth of Strained Crystals. *J. Cryst. Growth* **1975**, *28* (2), 249−253.
(40) Jow, T. R.; Zheng, J. P. Amorphous Thin Film Ruthenium Oxide as an Electrode Material for Electrochemical Capacitors. *MRS Proc.* **1995**, *393* (8), 433−438.
(41) Cheng, G.; Xu, J.; Dong, C.; Yang, W.; Kou, T.; Zhang, Z. Anodization Driven Synthesis of Nickel Oxalate Nanostructures with Excellent Performance for Asymmetric Supercapacitors. *J. Mater. Chem. A* **2014**, *2* (41), 17307−17313.
(42) Machoke, A. G. F.; Arias, A. M.; Baracchini, G.; Rubin, M.; Baser, H.; Weissenberger, T.; Dittmeyer, R.; Weber, A.; Hartmann, M.; Schwieger, W. MFI Type Zeolite Aggregates with Nanosized

https://doi.org/10.1021/acsomega.3c08012
ACS Omega 2023, 8, 45152−45162

Particles via a Combination of Spray Drying and Steam-Assisted Crystallization (SAC) Techniques. *Catalysts* **2023**, *13*, 536.
(43) Fievet, F.; Lagier, J. P.; Blin, B.; Beaudoin, B.; Figlarz, M. Homogeneous and Heterogeneous Nucleations in the Polyol Process for the Preparation of Micron and Submicron Size Metal Particles. *Solid State Ionics* **1989**, *32*−*33* (PART 1), 198−205.
(44) Wu, C. H.; Ma, J. S.; Lu, C. H. Synthesis and Characterization of Nickel-Manganese Oxide via the Hydrothermal Route for Electrochemical Capacitors. *Curr. Appl. Phys.* **2012**, *12* (4), 1190−1194.
(45) Liang, C. H.; Hwang, C. S. Effects of Temperatures and Cations of Electrolyte on the Capacitive Characteristics of the Manganese Oxide Deposited by Hydrothermal Electrochemical Method. *J. Alloys Compd.* **2010**, *500* (1), 102−107.
(46) Haris, M. F. L.; Yin, C. Y.; Jiang, Z. T.; Goh, B. M.; Chen, X.; Al-Masry, W. A.; Abukhalaf, A. M.; El-Harbawi, M.; Huang, N. M.; Lim, H. N. Crystallinity and Morphological Evolution of Hydrothermally Synthesized Potassium Manganese Oxide Nanowires. *Ceram. Int.* **2014**, *40* (1 PART A), 1245−1250.
(47) Dunne, P. W.; Munn, A. S.; Starkey, C. L.; Huddle, T. A.; Lester, E. H. Continuous-Flow Hydrothermal Synthesis for the Production of Inorganic Nanomaterials. *Philos. Trans. R. Soc. A* **2015**, *373*, No. 20150015.
(48) Liu, Z.; Wang, W.; Lou; Liu, X.; Wu, M.; Li, D.; Zeng, Z. Hydrothermal Synthesis of Nanostructured Spinel Lithium Manganese Oxide. *J. Solid State Chem.* **2004**, *177* (4−5), 1585−1591.
(49) Lester, E.; Aksomaityte, G.; Li, J.; Gomez, S.; Gonzalez-Gonzalez, J.; Poliakoff, M. Controlled Continuous Hydrothermal Synthesis of Cobalt Oxide (Co_3O_4) Nanoparticles. *Prog. Cryst. Growth Charact. Mater.* **2012**, *58* (1), 3−13.
(50) Malligavathy, M.; Iyyapushpam, S.; Nishanthi, S. T.; Padiyan, D. P. Role of Hydrothermal Temperature on Crystallinity, Photoluminescence, Photocatalytic and Gas Sensing Properties of TiO_2 Nanoparticles. *Pramana* **2018**, *90*, 44.
(51) Xia, K.; Liu, X.; Liu, H.; Li, W.; Li, Y.; Han, F.; Duan, L.; Hou, Z. Microwave-Assisted Solvothermal Synthesis of Hollow Mesoporous SiOC Ceramics in NaOH Solution. *Ceram. Int.* **2022**, *48* (13), 19232−19239.
(52) Yamada, Y.; Matsubara, M.; Muramatsu, A.; Takeda, S. ichi.; Kanie, K. Highly Concentrated Solvothermal Synthesis of Sub-10-nm $BaTiO_3$ Nanoparticles for Optical Applications. *Adv. Powder Technol.* **2022**, *33* (8), No. 103660.
(53) Deng, N.; Zhou, L.; Peng, X.; Wang, X.; Ge, H. Preparation and Characterization of Nickel-Zinc Ferrites by a Solvothermal Method. *Rare Met. Mater. Eng.* **2015**, *44* (9), 2126−2131.
(54) Thanh, N. T. K.; Maclean, N.; Mahiddine, S. Mechanisms of Nucleation and Growth of Nanoparticles in Solution. *Chem. Rev.* **2014**, *114* (15), 7610−7630.
(55) Polte, J. Fundamental Growth Principles of Colloidal Metal Nanoparticles - a New Perspective. *CrystEngComm* **2015**, *17* (36), 6809−6830.
(56) Oku, M. X-Ray Photoelectron Spectra of $KMnO_4$ and K_2MnO_4 Fractured in Situ. *J. Electron Spectrosc. Relat. Phenom.* **1995**, *74* (2), 135−148.
(57) Sukhdev, A.; Challa, M.; Narayani, L.; Manjunatha, A. S.; Deepthi, P. R.; Angadi, J. V.; Mohan Kumar, P.; Pasha, M. Synthesis, Phase Transformation, and Morphology of Hausmannite Mn_3O_4 Nanoparticles: Photocatalytic and Antibacterial Investigations. *Heliyon* **2020**, *6* (1), No. e03245.
(58) Ramírez, A.; Hillebrand, P.; Stellmach, D.; May, M. M.; Bogdanoff, P.; Fiechter, S. Evaluation of MnO_x, Mn_2O_3, and Mn_3O_4 Electrodeposited Films for the Oxygen Evolution Reaction of Water. *J. Phys. Chem. C* **2014**, *118* (26), 14073−14081.
(59) Biesinger, M. C.; Payne, B. P.; Grosvenor, A. P.; Lau, L. W. M.; Gerson, A. R.; Smart, R. S. C. Resolving Surface Chemical States in XPS Analysis of First Row Transition Metals, Oxides and Hydroxides: Cr, Mn, Fe, Co and Ni. *Appl. Surf. Sci.* **2011**, *257* (7), 2717−2730.
(60) Pan, R.; Li, Y.; Fang, F.; Cao, W. Surface Valence States of Mn Ions and Magnetic Properties of $La_{0.67}Sr_{0.33}MnO_3$ Films. *Int. J. Mater. Sci. Appl.* **2016**, *5* (5), 222−227.
(61) Ilton, E. S.; Post, J. E.; Heaney, P. J.; Ling, F. T.; Kerisit, S. N. XPS Determination of Mn Oxidation States in Mn (Hydr)Oxides. *Appl. Surf. Sci.* **2016**, *366*, 475−485.
(62) Murray, J. W.; Dillard, J. G.; Giovanoli, R.; Moers, H.; Stumm, W. Oxidation of Mn(II): Initial Mineralogy, Oxidation State and Ageing. *Geochim. Cosmochim. Acta* **1985**, *49* (2), 463−470.
(63) Garcês Gonçalves, P. R.; De Abreu, H. A.; Duarte, H. A. Stability, Structural, and Electronic Properties of Hausmannite (Mn_3O_4) Surfaces and Their Interaction with Water. *J. Phys. Chem. C* **2018**, *122* (36), 20841−20849.
(64) Ma, C.; Wen, Y.; Yue, Q.; Li, A.; Fu, J.; Zhang, N.; Gai, H.; Zheng, J.; Chen, B. H. Oxygen-Vacancy-Promoted Catalytic Wet Air Oxidation of Phenol from MnO_x-CeO_2. *RSC Adv.* **2017**, *7* (43), 27079−27088.
(65) Yang, R.; Ren, C.; Teng, X.; Chen, Z.; Wu, S.; Zhang, W. Study of the Surface Oxygen Vacancies Evolvement on the Single and Bi-Components Manganese Oxide Precursors and Their Catalytic Performance. *Catal. Lett.* **2017**, *147* (3), 727−737.
(66) Divya, T.; Anjali, C.; Sunajadevi, K. R.; Anas, K.; Renuka, N. K. Influence of Hydrothermal Synthesis Conditions on Lattice Defects in Cerium Oxide. *J. Solid State Chem.* **2021**, *300* (May), No. 122253.
(67) Trovarelli, A. Catalytic Properties of Ceria-Containing Materials. *Catal. Rev.* **1996**, *38* (4), 439−520.
(68) Barbero, B. P.; Gamboa, J. A.; Cadús, L. E. Synthesis and Characterisation of La1-XCaxFeO3 Perovskite-Type Oxide Catalysts for Total Oxidation of Volatile Organic Compounds. *Appl. Catal., B* **2006**, *65* (1−2), 21−30.

https://doi.org/10.1021/acsomega.3c08012
ACS Omega 2023, 8, 45152−45162